

Quantifying symmetric exchange in ultrathin ferromagnetic films with chirality

Tobias Böttcher,^{1,2} Xiaoye Chen,³ Banibrato Sinha,^{1,*} T S Suraj,⁴ Hui Ru Tan,³ Hang Khume Tan,³ Burkard Hillebrands,¹ Mikhail Kostylev,⁵ Robert Laskowski,⁶ Khoong Hong Khoo,⁶ Anjan Soumyanarayanan,^{3,4,†} and Philipp Pirro^{1,†}

¹ Fachbereich Physik and Landesforschungszentrum OPTIMAS,

Technische Universität Kaiserslautern, Gottlieb-Daimler-Straße 46, 67663 Kaiserslautern, Germany

² MAINZ Graduate School of Excellence, Staudingerweg 9, 55128 Mainz, Germany

³ Institute of Materials Research and Engineering, Agency for Science, Technology and Research, 2 Fusionopolis Way, 138634, Singapore

⁴ Department of Physics, National University of Singapore, 2 Science Drive 3, 117551, Singapore

⁵ School of Physics, M013, University of Western Australia, Crawley, Perth 6009, Western Australia, Australia

⁶ Institute of High Performance Computing, Agency for Science,

Technology and Research, 1 Fusionopolis Way, Connexis, Singapore 138632, Singapore

(Dated: September 10, 2021)

Determining symmetric (Heisenberg) exchange in an ultrathin magnetic film is challenging because all known experimental methods require knowledge of several other material parameters. We present and compare results of different methods based on the probing of spin waves to determine the symmetric exchange in a series of Co/Pt-based ultrathin magnetic films, hosting varying extents of chirality. The first is Brillouin light scattering spectroscopy which allows us to study the spin-wave spectrum near the Brillouin zone origin. In addition, systematic measurements of the saturation magnetization as a function of temperature $M_S(T)$ are utilized, which effectively probe the population of the spin-wave spectrum over a significant part of the Brillouin zone. Here, different models are applied and discussed in the view of the thin film character of the samples and an analysis of the spin-wave density of states is employed to evaluate limitations of theoretical $M_S(T)$ models. We compare the experimental results to *ab initio* density functional theory calculations. Although qualitative trends are apparent, we note significant differences in the absolute values of the exchange constants obtained by the various methods. Our results elucidate the origin of the large scatter in exchange constants reported in the literature for nominally very similar thin film systems. We find and explain that $M_S(T)$ -based methods tend to give lower values for the symmetric exchange compared to an analysis of the dispersion relation close to the Brillouin zone origin. Given the importance of the symmetric exchange for applications of magnetic thin films, we hope our findings proof useful when it comes to the characterization of other thin film systems.

I. INTRODUCTION

CMOS-based devices have rendered possible a rapid development of information processing technology over the past decades, which can well be described by Moore’s law [1, 2]. Based on a continuous decrease of device size [3], however, further improvement comes not only with increasing technological and financial challenges, but also, in connection with Joule heating, critical power densities are being approached. In this context, spintronics is considered to form the basis of a new generation of information processing and storage devices [4–10]. The development of this technology requires a fundamental understanding and accurate measurement of the properties of the material systems used, which usually are in the ultrathin film domain.

For example, such material parameters as symmetric and antisymmetric (Dzyaloshinskii-Moriya) exchange in-

teraction play a vital role in determining the characteristics of skyrmions, which are envisaged as spintronic information carriers [11]. While much effort has been made in the investigation and understanding of the interfacial Dzyaloshinskii-Moriya interaction (DMI) [12–14], which is a critical parameter for the properties of skyrmions, much less attention is devoted to the peculiarities of Heisenberg exchange interaction in skyrmion-hosting systems.

One such system consists of Co/Pt-based multilayers, which are shown to host chiral magnetic textures upon the introduction of stack asymmetry, e.g. via an additional heavy metal (Ir, Ta, etc.) [14–16]. Also, a precise measurement of exchange constant is equally important for advances in the field of magnonics [17].

In this work, we present and compare results of Heisenberg exchange determination in ultrathin magnetic films using various methods. Based on Brillouin light scattering (BLS) spectroscopy measurements, a detailed analysis of the spin-wave dispersion relation for wave vectors close to the Brillouin zone origin has been performed and the Heisenberg exchange constant A has been extracted. At the same time, magnetometry measurements analyzed with different variants for the Bloch model adapted to ul-

* Current affiliation: Department of Applied Physics, Northwestern University, Evanston, IL 60208, USA

† Corresponding authors:
anjan@imre.a-star.edu.sg, ppirro@physik.uni-kl.de

trathin films are used to extract the Heisenberg exchange constant in a second, independent manner. This second technique effectively probes spin waves over a large part of the Brillouin zone. Furthermore, microscopic domain periodicity measurements, which measure the ratio of symmetric and antisymmetric exchange interaction are also performed, and, eventually, DFT calculations are used for comparison with the experimental results. Although qualitative trends are apparent, we note that there are significant differences in the absolute values of the exchange constants obtained by the various methods. We discuss the strengths, weaknesses and limitations of the individual techniques. Based on these findings, experimental requirements and consequences are discussed.

The manuscript is structured as follows: In Section II, we give a short summary of the basis of the different methods used, and in Section III, we present the results of these methods applied to a set of five different thin-film samples. A comparison and conclusion is given in Section IV.

II. METHODS FOR EXCHANGE DETERMINATION

Spin-wave dispersion analysis based on Brillouin light scattering spectroscopy

The dispersion relation of spin waves in magnetic thin films, accessible to BLS spectroscopy, can be used to quantify the parent exchange interactions at room temperature [18]. BLS spectroscopy is based on the inelastic scattering of photons with magnons and is an established method for the experimental investigation of spin waves in magnetic thin films for wave vectors up to approx. 25 rad/μm. Its ability to detect thermal spin waves in ultrathin magnetic films with capping layers in the nanometer range distinguishes it from neutron scattering and inelastic spin-polarized electron scattering techniques. A detailed description of this method can be found, for instance, in Sebastian *et al.* [19]. Technical details of the setup used in this work are specified in the Appendix.

Notably, in recent years, BLS spectroscopy has been used extensively to measure the interfacial DMI in chiral multilayers [20–23]. In contrast, the corresponding symmetric exchange interaction has received scant attention from the technique, likely due to the concomitant presence of interlayer interactions – absent in this work.

The dispersion relation of spin waves propagating perpendicular to the static magnetization in the plane of a homogeneously, in-plane saturated ultrathin film can be treated within the description by Kalinikos and Slavin [24]. Interfacial DMI leads to an asymmetry of the spin-wave dispersion linear in the spin-wave wave vector [20]. In turn, the symmetric part of the spin-wave dispersion allows for an extraction of the Heisenberg exchange con-

stant [18] and is described by the relation [21]

$$\begin{aligned} f(k)_{\text{sym}} &= (f_{\text{sw}}(k) + f_{\text{sw}}(-k)) / 2 \\ &= \frac{\gamma \mu_0}{2\pi} \left[\left(H_{\text{ext}} + \lambda_{\text{ex}} k^2 + M_S g(kt) \right) \right. \\ &\quad \left. \cdot \left(H_{\text{ext}} - H_U + \lambda_{\text{ex}} k^2 + M_S (1 - g(kt)) \right) \right]^{1/2}, \end{aligned} \quad (1)$$

where the gyromagnetic ratio, $\gamma = 176 \text{ rad T}^{-1} \text{ ns}^{-1}$ for this work, t is the film thickness, $\mu_0 H_U$ is the uniaxial anisotropy field, and M_S is the saturation magnetization of the material. The influence of the symmetric exchange is contained in the spin-wave stiffness $\lambda_{\text{ex}} = 2A/(\mu_0 M_S)$ with the Heisenberg exchange constant A . In addition, the term $g(x) = 1 - [1 - \exp(|x|)] / |x|$ accounts for the dipolar interaction between magnetic moments. The challenge to determine A with the help of this relation lies in the correct consideration of the further contributing terms like the dipolar interaction and the anisotropy. In particular, the method requires a good knowledge of the saturation magnetization, which usually has to be measured using additional methods.

Concerning the bilayer character of one of the samples, numerical calculations [25] and numerical modeling [26] are valuable methods for understanding the spin-wave dispersion relation in such systems. To be able to model the effect of the ferromagnetic bilayer Fe/Co and its effective exchange constant A , we compare Eq. (1) to an advanced modeling of the dispersion relation by the method described in the work by Kostylev [26]. It implements a numerical solution of the integro-differential equation describing the boundary condition problem and allows to calculate the dispersion relation for a thin film with arbitrary distribution of M_S , H_U , and A over the film thickness. Specifically, based on this modeling, we have verified that the spin-wave dispersion relation in ultrathin bilayers of two ferromagnetic metals like Fe and Co can be described using an effective exchange spin-wave stiffness (see Appendix). This enables us to model the bilayer sample as an effective single layer in order to ensure compatibility with the theoretical models presented above. Our purely theoretical analysis shows that, for a bilayer, the dispersion relation for the exchange-dominated spin waves can be described by the effective curvature of the dispersion β :

$$f_{\text{sw}}(k) = \frac{\gamma}{\pi} \frac{A}{M_S} \cdot k^2 = \beta \cdot k^2 \quad (2)$$

$$\beta = \frac{\gamma}{\pi} \frac{A_{\text{Fe}} \cdot t_{\text{Fe}} + A_{\text{Co}} \cdot t_{\text{Co}}}{M_S^{(\text{Fe})} \cdot t_{\text{Fe}} + M_S^{(\text{Co})} \cdot t_{\text{Co}}}. \quad (3)$$

Here, A_{Fe} and A_{Co} denote the exchange constants of Fe and Co, respectively, and t_{Fe} and t_{Co} denote the thicknesses of the respective layers with particular saturation magnetizations $M_S^{(\text{Fe})}$ and $M_S^{(\text{Co})}$.

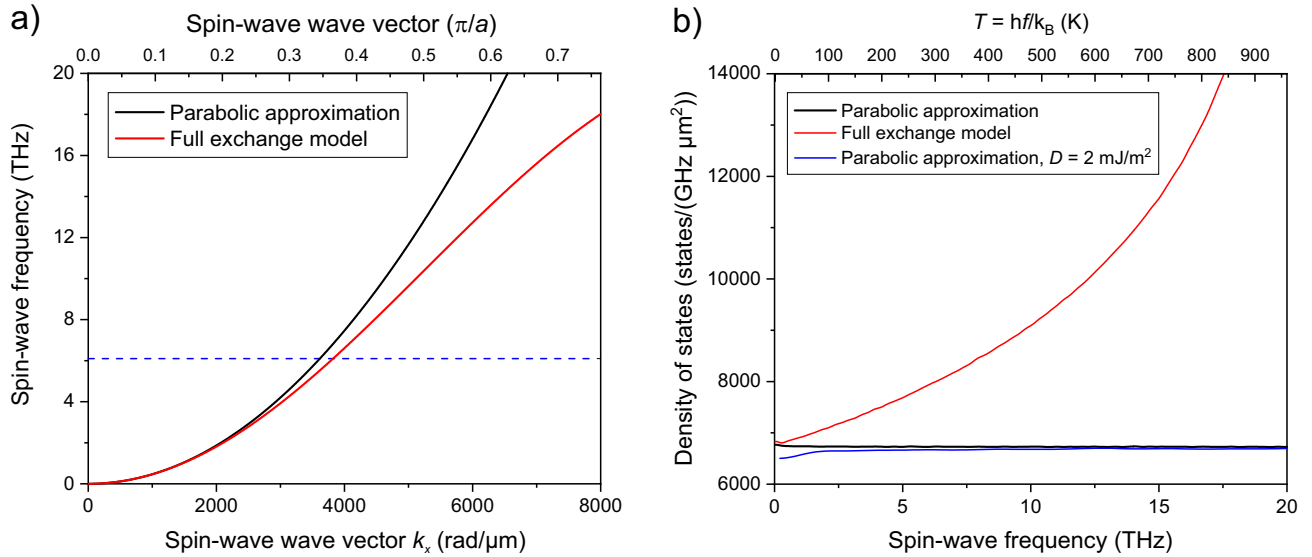


Figure 1. a) Full dispersion relation (red solid line) and quadratic approximation (black solid line) for spin waves propagating along the x direction (cf. model according to Eqs. (13) and (14) in the Appendix). Dispersion models and calculation parameters are given in the main text. The blue dashed line is at $f = k_B T/h$ with $T = 293 \text{ K}$. b) Numerical evaluation of the spin-wave density of states for different dispersion models in a 2D system. The black line is the DOS for the parabolic dispersion model and the red line is the DOS for the full exchange model. The blue line is the DOS for a parabolic dispersion approximation for an in-plane saturated film including a DMI-induced asymmetry resulting from an iDMI constant of 2 mJ/m^2 .

Temperature dependence of saturation magnetization

The temperature dependence of the saturation magnetization $M_S(T)$ of a material, measured using widely accessible magnetometry techniques, can be analyzed to extract the exchange constant [27–29]. Given its extensive use for quantifying exchange in chiral magnetic thin films [22, 23], here we examine this technique and present an overview of possible analysis approaches. For small temperatures, $M_S(T)$ is mainly a result of the excitation of thermal spin waves. This can be seen as related to a dispersion analysis with the spin-wave frequency extending into the THz range and thermal population of the states described by Bose-Einstein statistics. For the theoretical analysis, the underlying dispersion model and the associated spin-wave density of states $\rho(\omega)$ play an important role, where ω is the spin-wave frequency. Assuming a parabolic dispersion model $\omega(k) = \gamma\mu_0\lambda_{\text{ex}} \cdot k^2 = 2\gamma(A/M_S) \cdot k^2$ for a three-dimensional, extended bulk sample (resulting in a spin-wave density of states $\rho(\omega) \propto \sqrt{\omega}$) and thus neglecting any influence of dipolar interactions, anisotropies, or DMI on the dispersion relation, leads to the well known Bloch $T^{3/2}$ law given by [30, 31]

$$M(T)_{S,T^{3/2}} = M_S(0) - 2\mu_B \cdot \eta \cdot \left(\frac{k_B T M_S(0)}{2\gamma A \hbar} \right)^{3/2}, \quad (4)$$

where $M_S(0)$ is the saturation magnetization at zero temperature and η is a dimensionless prefactor. It is particularly suitable for describing the temperature dependence

of the magnetization of bulk samples at low temperatures (where single particle excitations can be neglected [32]) in which case $\eta = 0.0587$ [29, 31]. Notably, in this case, the absolute value of $M_S(0)$ is needed to obtain A from a fit to Eq. (4). However, some have found Bloch's $T^{3/2}$ law to be less adequate for the treatment of data obtained in the ultrathin film regime under consideration in this work because of the reduced, two-dimensional character strongly influencing the spin-wave density of states [22, 28, 33]. Some attempts have been made to employ a modified Bloch law [22, 34, 35], for instance, a modification of the factor η in Eq. (4) to take into account the altered magnon density in such systems [22]. In this case, however, the $T^{3/2}$ dependence typical for 3D systems is conserved and a generalization of this approach seems difficult. For a film thickness of 1 nm, $\eta \approx 0.3$ is found for NiFe which we use as a trial for the extraction of the exchange constant in the following section (For $t = 2 \text{ nm}$, $\eta \approx 0.17$ [22]).

A more direct approach for ultrathin films has been proposed, which directly includes the 2D nature of the system into the $M_S(T)$ expression [31]. As a first approach for ultrathin films, it appears sufficient to limit considerations to the fundamental spin-wave mode only (homogeneous mode profile over the film thickness), which is the basis of the 2D model with the dispersion given by $\omega(k) = \omega_0 + 2\gamma A/M_S(0)k^2$ [31]. In this case, $\rho(\omega)$ is a constant with $\rho(\omega)$ proportional to $M_S(0)/A$. The inclusion of a finite spin-wave frequency gap ω_0 , which results from dipolar interactions, anisotropies and external magnetic fields, is indispensable to model a finite M_S for $T > 0$ (Mermin-Wagner theorem [36]). The

calculation then results in [31]

$$M_S(T)_{2D} = M_S(0) \left[1 - \frac{\mu_B k_B T}{4\pi\gamma A \hbar} \ln \left(\frac{k_B T}{\hbar\omega_0} \right) \right]. \quad (5)$$

Here, a fitting of A to $M_S(T)$ requires knowledge of the film thickness, but is independent of $M_S(0)$. Importantly, the 2D model needs to be improved if thickness modes are significantly populated[33]. Even for films with a thickness of a few nanometers only, the thermal population of perpendicular standing spin-wave (PSSW) modes can play a role for temperatures usually used in magnetometry. An estimate for their contribution can be given by considering the Bose-Einstein distribution $N(\omega)$ with

$$N(\omega) = \frac{1}{\exp\left(\frac{\hbar\omega}{k_B T}\right) - 1}. \quad (6)$$

Assuming $t = 2$ nm, $M_S = 1200$ kA/m, and $A = 6$ pJ/m, we estimate for the frequency of the first PSSW mode with a wave vector component $k_\perp^{(1)} = \pi/t$ perpendicular to the film plane $\omega_1 \approx 2\pi \cdot 1.3$ THz and for the second PSSW mode ($k_\perp^{(2)} = 2\pi/t$) $\omega_2 \approx 2\pi \cdot 5.5$ THz. Hence, assuming $\omega_0 \approx 2\pi \cdot 20$ GHz for the fundamental mode, the relative occupation at room temperature of the PSSW modes is $N(\omega_1)/N(\omega_0) = 1.3\%$ and $N(\omega_2)/N(\omega_0) = 0.2\%$ and higher modes have an even lower occupation. Thus, while it appears necessary to take standing spin-wave modes into account in order to describe the temperature-dependent reduction of M_S with adequate precision, an inclusion of the first two PSSW modes is sufficient. Neglecting these modes or, in other words, applying a pure 2D model, leads to an underestimation of the magnon density and, consequently, of the magnetization reduction with increasing temperature, such that a smaller exchange constant seemingly suffices to stabilize the ferromagnetic order at elevated temperatures.

The contribution of the thermal population of the PSSW modes to the reduction of the magnetization can straightforwardly be considered by utilizing a model accounting for the influence of each mode separately [28, 31]. Including the fundamental mode as well as the PSSW modes of first and second order, the temperature-induced reduction of the magnetization can be described by [28, 31]

$$M_S(T)_{\text{PSSW}} = M_S(0) \left[1 - \sum_{n=0}^2 \frac{\mu_B k_B T}{4\pi\gamma A \hbar} \ln \left(\frac{\exp(\hbar\omega_n/k_B T)}{\exp(\hbar\omega_n/k_B T) - 1} \right) \right]. \quad (7)$$

As the spin-wave dispersion relation, however, deviates from the assumed parabolic shape towards the Brillouin zone boundary, all presented approaches are only valid at low temperatures for which the thermal excitation of high wave vector magnon states can be neglected. This fact can well be illustrated for the 2D case by taking a

closer look on the spin-wave density of states, which directly governs the temperature-dependent reduction of the magnetization. A detailed discussion of this situation is presented in the Appendix. The essential idea is captured in Fig. 1a), in which two spin-wave dispersion models for a 2D square lattice are shown. Both curves have been calculated using $\omega_0 = 2\pi \cdot 10$ GHz, $M_S = 1200$ kA/m, $A = 10$ pJ/m, and a lattice constant of $a = 3$ Å to model the behaviour of typical ultrathin metallic ferromagnets [29]. The red line is a plot of the full dispersion relation whereas the black line represents the parabolic approximation, Eq. (5). The blue dashed line with $f = k_B T/h$ evaluated at room temperature serves as an indication for the maximum thermal population of the spin-wave states reached in our magnetometry measurements. The implications of using the approximate parabolic model when evaluating the spin-wave density of states for the Bloch law become evident in Fig. 1b). While the parabolic approximation results in a constant DOS, the full model leads to a DOS increasing with the spin-wave frequency. Consequently, as temperature increases, more states of higher frequency become populated and with the increasingly larger DOS in the full model, $M_S(T)$ decreases faster than predicted within the parabolic model. As a result, any model for the temperature dependence of the magnetization based on the parabolic dispersion approximation suffers from an underestimation of the actual spin-wave DOS and, hence, underestimates the corresponding magnetization reduction. This leads to the prediction of a larger M_S for a given A and T such that these models generally underestimate the actual exchange constant A of the system since the exchange stabilizes the ferromagnetic order against thermal fluctuations.

At the same time, the DOS is only insignificantly altered if the influence of an interfacial DMI on the spin-wave dispersion relation is included as becomes clear from the blue curve in Fig. 1b), which shows the DOS assuming $D = 2$ mJ/m². Hence, we predict that for experimental $M_S(T)$ measurements for thin films both the in-plane and out-of-plane field configuration can be treated equally to good approximation.

In the context of the analysis of the temperature dependence of the magnetization it is important to also point out the fact that Bloch's $T^{3/2}$ law as well as the other models deliver values for the exchange constant at zero temperature [22, 29], thus requiring a renormalization of the exchange constant to room temperature. Based on *ab initio* calculations, Moreno *et al.* [37] have found the scaling relation $A \propto M_S^{1.8}$ such that the renormalization of the exchange constant to room temperature can be performed using the relation

$$A(T = RT) = A(0\text{ K}) \cdot \left(\frac{M_S(T = RT)}{M_S(0\text{ K})} \right)^{1.8}. \quad (8)$$

Domain periodicity

In chiral multilayers where the microscopic domain characteristics are dominated by the competition between D and A , we can compare experimentally-measured domain periodicity at remanence with micromagnetic simulations to determine the ratio of A and D . An independent determination of D can then be used to extract the exchange constant [14, 15].

In this work, domain periodicity measurements are performed using Lorentz transmission electron microscopy (LTEM) details of which are described in the Appendix. Meanwhile, micromagnetic simulations are performed for M_S and uniaxial anisotropy (K_u) parameters obtained from magnetometry, and for a matrix of D and A values. Subsequently, the real space magnetization of each simulation is Fourier-transformed to extract the period (P), which is then fitted to a low-order 2D polynomial: $P = a_0 + a_1 D + a_2 A + a_3 D \cdot A$. Finally, by constraining the fit with experimental period and D from BLS spectroscopy, A can be determined.

DFT calculations

To complement the experimental results, density functional theory calculations have been performed to extract A [38, 39]. The simulations are performed on slabs with compositions PtCo_5Pt , IrCo_5Pt , and $\text{IrFe}_2\text{Co}_3\text{Pt}$, where the subscripts for Fe (Co) represent the number of atomic layers. As each Fe (Co) atomic layer is about 0.2 nm thick, these correspond to experimental thicknesses of Pt/Co(1)/Pt , Ir/Co(1)/Pt , and $\text{Ir/Fe(0.4)/Co(0.6)/Pt}$. Each slab is separated by a vacuum of 10 Å in the normal direction to prevent spurious intercell interactions, and the in-plane lattice constant is set to the bulk Ir value with exchange-correlation approximated by the Perdew-Burke-Ernzerhof formulation of GGA [40]. The generalized Bloch's theorem is used to generate spin spirals with q -vectors directed along the direction of the in-plane nearest neighbor atom, and the spiral axis is given by the cross product of the q -vector and slab normal with a spiral angle of 90° [39, 41]. To extract the exchange constant A , the spiral energy density is calculated over a range of wave vectors q and fit to a quadratic function. In terms of accuracy, these methods have been assessed in previous works and shown to be fairly accurate and capable of predicting trends obtained from experimental results [42].

III. RESULTS

The values for the exchange constant extracted from different techniques are summarized in Table I and plotted in Fig. 6. In the following, after introducing the samples under investigation, we discuss the results of the specific methods.

Samples

In total, five ultrathin sample compositions — Pt/Co(1)/Pt , Ir/Co(1)/Pt , $\text{Ir/Fe(0.4)/Co(0.6)/Pt}$, Pt/Co(2)/Pt , Ir/Co(2)/Pt — are examined in this work, prepared by magnetron sputtering. Ferromagnet layer thicknesses, in nm, are indicated in parentheses, and the full stack details are provided in Section V.

This sample set is designed to compare the effects of inversion symmetry (Pt/Co/Pt vs the rest), ferromagnetic bilayer ($\text{Ir/Fe(0.4)/Co(0.6)/Pt}$ vs Ir/Co(1)/Pt), and varying ferromagnet thickness (Co(1) vs Co(2)) on exchange interaction and its experimental determination.

BLS spectroscopy and dispersion analysis

In the BLS dispersion measurements, for all samples the externally applied field is chosen such that the magnetic film is saturated in its plane. Thus, thermally populated magnetostatic surface spin waves described by Eq. (1) are probed, which, in the specific BLS setup geometry, propagate perpendicularly to the applied field. Figure 2 exemplarily shows the dispersion data obtained from BLS measurements for two films along with the modeled dispersion based on the numerical code. For the $\text{Ir/Fe(0.4)/Co(0.6)/Pt}$ sample, the measurement has been performed at an applied field of $\mu_0 H_{\text{ext}} = 300$ mT and the value used for the saturation magnetization in numerical modeling is $M_S = 1228$ kA/m, as obtained from vibrating sample magnetometry (VSM) measurements. Good agreement with the experimental data is achieved for $A = 7$ pJ/m and a uniaxial anisotropy field of $\mu_0 H_U = 1433$ mT. The error bars given for A from the dispersion analysis have been estimated as follows: First, it needs to be pointed out that both the symmetric exchange and the anisotropy field, $\mu_0 H_U$ affect the curvature of the dispersion relation. Hence, we vary the symmetric exchange A and balance the resulting modification of the curvature of the dispersion relation by a modification of the anisotropy field. Since the FMR frequency (ω_0) sensitively depends on the anisotropy field, this requires an adaption of the saturation magnetization, M_S . We allow for a variation of the symmetric exchange until a modification of M_S of about 15 % is reached corresponding to the uncertainty of the VSM measurements used to determine M_S which then gives the limits for the value of the symmetric exchange.

Similarly, for the Ir/Co(1 nm)/Pt film, the measurement has been performed at an applied field of $\mu_0 H_{\text{ext}} = 830$ mT. The dispersion data, which shows a much larger slope compared to the previous case, is reproduced setting model parameters of $M_S = 1177$ kA/m, $A = 22$ pJ/m, and $\mu_0 H_U = 2210$ mT. Similar modeling has been applied to all other samples and the results are summarized in Fig. 6. The corresponding values can be found in Table I in the Appendix.

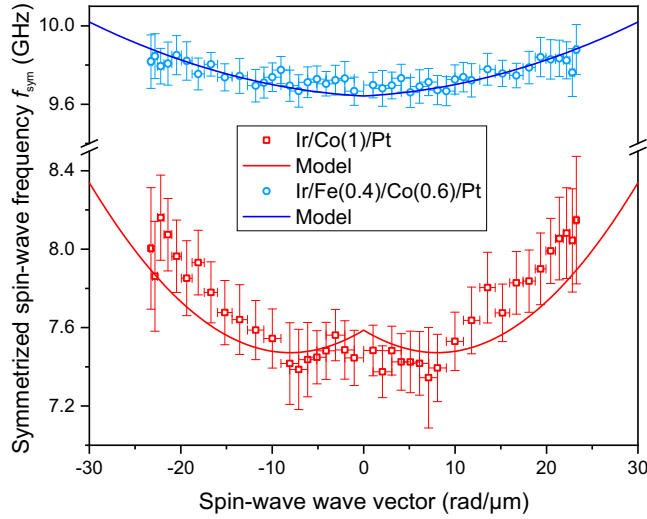


Figure 2. Symmetric part of the spin-wave dispersion relation (f_{sym} , Eq. (1)) obtained based on wave-vector resolved BLS spectroscopy (blue circles and red squares) and numerical model (solid lines). Blue circles and blue solid line are for the magnetic bilayer sample stack Ir/Fe(0.4 nm)/Co(0.6 nm)/Pt and red squares and red solid line are for the Ir/Co(1 nm)/Pt film.

$M_S(T)$ results and data analysis

Figure 3 exemplarily shows the $M_S(T)$ data obtained from the Ir/Fe(0.4)/Co(0.6)/Pt and Ir/Co(1)/Pt sample using SQUID magnetometry measurements. We have performed such measurements with the field applied along the sample normal and in the plane of the film and no significant difference between the resulting exchange values has been found. This is in line with the discussion of the negligible influence of the DMI on the spin-wave DOS in the previous section. As an alternative approach, we have also performed direct measurements of the magnetization as a function of temperature at fixed applied field. While this allows for a more precise estimation of ω_0 in Eq. (7), we find excellent agreement of the obtained values for A with the measurement method in which the field is swept. A more detailed description and comparison is given in the Appendix.

The data were fit using Bloch's $T^{3/2}$ law with the 3D value for η , the thickness corrected η values mentioned in the method section as well as the $M_S(T)$ dependence including the contribution from PSSW modes given by Eq. (7), which is represented in Fig. 3 by the solid blue lines and the dashed green lines, respectively. For fitting Eq. (7), the center value of the covered field range ($\mu_0 H_{\text{ext}}$) was used to estimate $\omega_0 = \gamma \mu_0 (H_{\text{ext}} + H_U - M_S)$ [43], in which H_U has been extracted from BLS data and we have used the M_S value estimated from an extrapolation of the $M_S(T)$ data towards zero temperature. The frequency ω_0 is then used in Eq. (7) in order to extract the Heisenberg exchange constant. We perform the following iterative procedure to take into account that the starting

frequencies ω_1 and ω_2 of the PSSW themselves depend on the exchange A : Initially, the minimum frequency ω_0 of the fundamental mode is estimated. Based on that, the strict 2D model with Eq. (5) is evaluated. This leads to a lower estimate of the Heisenberg exchange, which we then, in combination with the saturation magnetization value from the extrapolation of $M_S(T)$ data towards zero temperature and the respective film thickness, use to calculate the frequencies ω_1 and ω_2 . These frequencies are taken to fit the more precise model in Eq. (7) up to $n = 2$ to the data. We iterate this fit twice involving the recalculated PSSW frequencies based on the respective obtained exchange constant and find a variation of the resulting exchange constant from the second to the third iteration below 1%.

With the field oriented along the film normal, any DMI-induced nonreciprocity in the spin-wave dispersion relation can be excluded, which is the basis of the $M_S(T)$ models in Eqs. (4) and (7). Nevertheless, as described above and in the Appendix, the influence of the DMI on the spin-wave dispersion relation for the in-plane field configuration does not significantly alter the results, as we have experimentally verified.

As becomes obvious from the Fig. 6, the exchange constants extracted using the version of Bloch's law with modified η ($t = 1$ nm, $\eta \approx 0.3$, $t = 2$ nm, $\eta \approx 0.17$ [22]) returns the highest values for A which agree best with the ones extracted from BLS and DFT.

The obtained exchange constants renormalized to room temperature (see Eq. (8)) are plotted in Fig. 6. The corresponding numerical values are given in Table I in the Appendix.

DFT calculations

Through our calculations, we obtained the spin spiral energy densities for PtCo₅Pt, IrCo₅Pt and IrFe₂Co₃Pt with wavevectors up to $\sim 0.6 \text{ \AA}^{-1}$ as shown in Fig. 4. The spiral energy shows approximate quadratic dependence on q with increasing deviation from parabolic behavior at large q . In addition, there is appreciable softening of the spin spiral for IrFe₂Co₃Pt at $q \sim 0.08 \text{ \AA}^{-1}$, a phenomenon also observed in IrFe slabs and attributed to hybridization between Ir and Fe [44]. We find that exchange is largest for slabs with pure Co layers and decreases with increasing Fe content. This is consistent with bulk Fe having lower exchange coupling than bulk Co. Also, the exchange stiffness is not strongly dependent on the heavy metal layers as it is mostly a ferromagnet property and this is demonstrated by the similar energies of PtCo₅Pt and IrCo₅Pt. To extract the exchange stiffness A , we fit the DFT spiral energy densities to a quadratic in q and we did it over different ranges of q . For small q , we fit to energies with $q < 0.12 \text{ \AA}^{-1}$ while for large q we fit to all energy points shown in Fig. 4. Due to the deviation from parabolicity, we obtain different values of A , with fit to small q yielding values of 17.4, 17.8 and

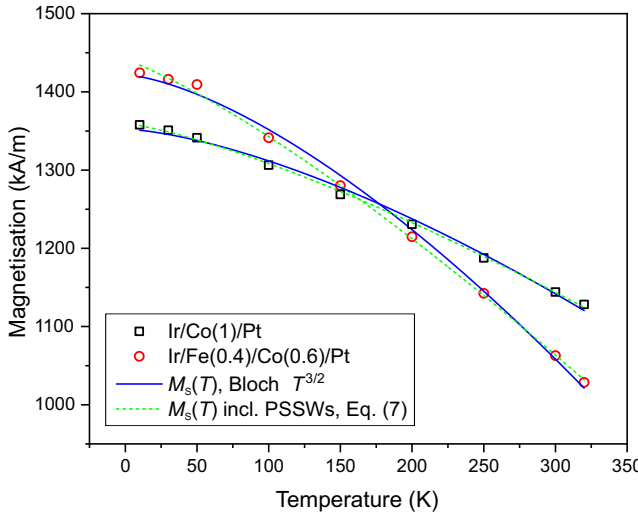


Figure 3. Magnetization as a function of temperature for the Ir/Co(1)/Pt film (black squares) and the Ir/Fe(0.4)/Co(0.6)/Pt film (red dots) determined from SQUID measurements. Data have been obtained from $M(H)$ measurements and an extrapolation towards zero field. Blue solid lines are fits to Bloch's $T^{3/2}$ law and green dashed lines are fits to Eq. (7) in the third iteration as discussed in the main text. The quicker decline observed for the Fe/Co bilayer sample is a consequence of the lower Heisenberg exchange observed for this sample.

13.6 pJ/m and that for large q giving values of 14.9, 14.0 and 6.7 pJ/m for PtCo₅Pt, IrCo₅Pt and IrFe₂Co₃Pt, respectively. As expected, IrFe₂Co₃Pt gives the smallest A while PtCo₅Pt and IrCo₅Pt give very similar A . Also, the exchange stiffness extracted for small q are consistently larger than that obtained over a larger range of q . This effect is particularly strong for IrFe₂Co₃Pt and is reasonable considering that spin spiral dispersion tends to flatten out as one approaches Brillouin zone boundaries. These results are also consistent with the trend in measured A with BLS yielding larger values of A than those obtained from magnetization measurements as discussed later in detail.

Domain periodicity

We used Lorentz transmission electron microscopy (LTEM) to image the magnetic texture at remanence (5a). In order to achieve sufficient magnetic contrast, a two-repeat version of Ir/Fe(0.4)/Co(0.6)/Pt is measured, and the period obtained is 87 nm. Micromagnetic simulations were performed with MuMax3 [45] for a matrix of D and A values (5b,c) and fitted well to a 2D polynomial ($R^2 = 0.99$). Constraining with experimentally-measured period and $D = 1.72$ mJ/m², $A = 11.1$ pJ/m. This analysis could not be performed for Pt/Co(1)/Pt and Ir/Co(1)/Pt, because of their high remanence magnetization, as also for the Co(2) samples, due to their

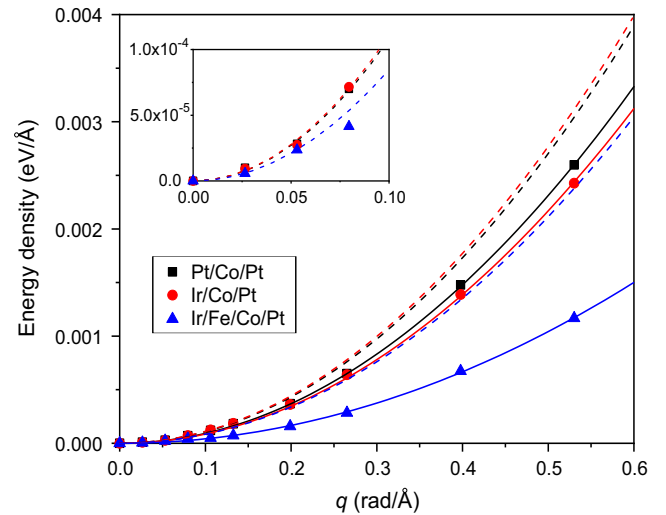


Figure 4. Spin spiral energy densities computed from DFT. The inset shows expanded view for small q region and solid and dashed lines are fits to quadratic function in q for small and large q values, respectively.

in-plane easy axis, both of which resulted in the lack of domain nucleation at remanence.

IV. DISCUSSION AND CONCLUSION

When comparing the values obtained using different methods and samples (see Fig. 6 and Table I), we have to state that for most of the samples, the values obtained with the different methods do not coincide within the errors bars. These are particularly large for the BLS measurements since many parameters with different dependencies are included. The other error estimations are based on the uncertainty of the parameters used in the respective fitting equations. We conclude that the deviations are probably of systematic nature and related to the different assumptions and limitations of the used methods as discussed in the manuscript and below. This could also explain to some degree the large spread of values reported for A in ultrathin films of very similar composition and thickness [23, 29, 31, 46, 47].

However, we identified an important qualitative trend: for a given films thickness, we can state that the relative evolution of A with the variation of the sample composition is very similar for all measurement methods. For the samples with 1 nm thickness for example, all methods measure the highest A for Pt/Co/Pt followed by Ir/Co/Pt and the lowest A is always obtained for Ir/Fe/Co/Pt. The decrease in A when Fe is present in the stack is in good qualitative agreement with the DFT results.

Concerning the values for A obtained for any particular sample, the BLS analysis consistently provides the largest value for A , followed by the Bloch law with modified η for thin films and the 2D Bloch law including

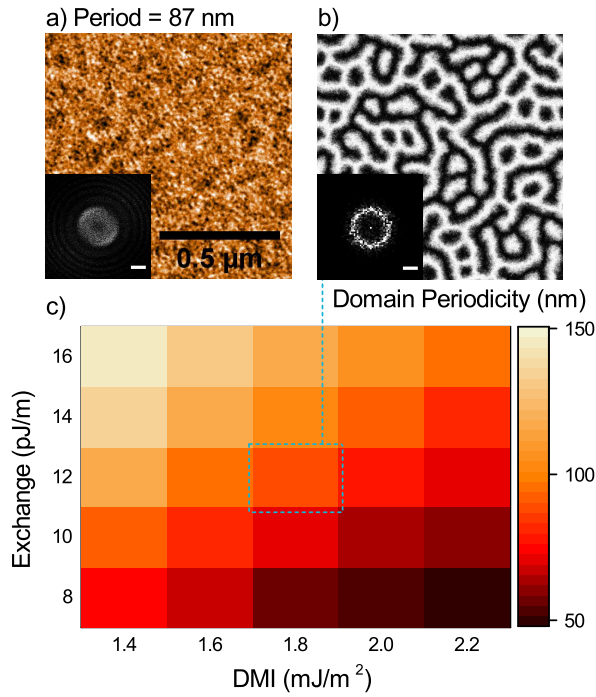


Figure 5. Domain periodicity analysis of the $[\text{Ir}(1)/\text{Fe}(0.4)/\text{Co}(0.6)/\text{Pt}(1)]_2$ sample, where the layer thicknesses, in nm, are indicated in parentheses. a) LTEM microscopy image at zero field. The insets of a), b) show the respective power spectra, scalebar: $10 \mu\text{m}^{-1}$. Despite the weak signal in real space, the signature ‘split-ring’ structure of LTEM is clear in frequency space, which allows us to obtain a period of 87 nm. b) M_z component of micromagnetic simulation with the closest D and A parameters. Same scale as a). c) Simulation period for a matrix of D and A values.

the PSSW modes (Eq. (7)). The original Bloch $T^{3/2}$ law (Eq. (4)) for 3D systems leads to the smallest value when applied to the thin films. Those values can be considered as unrealistically low since the 3D Bloch law does not take into account the increase of the magnon density in ultrathin films [22]. We presume that the iterative use of Eq. (7) results in values closer to the ones obtained from DFT calculations and based on BLS data. In fact, larger exchange values are found when employing the model including PSSW modes. Nevertheless, we also observe here in most cases a much smaller exchange constant compared to the direct measurement of the dispersion relation with BLS. A similar trend is observed for the Bloch $T^{3/2}$ law with thickness-corrected η .

The fact that all $M_S(T)$ -based methods lead to comparably low values for A could be attributed to several reasons. One is clearly the assumed parabolic approximation of the dispersion relation already discussed above, which generally leads to an underestimation of A in comparison to, e.g., the full Heisenberg model. The deviation from the parabolic dispersion relation does not play a significant role for the wave-vector range probed by BLS, but it is significant for the thermal spin-wave dis-

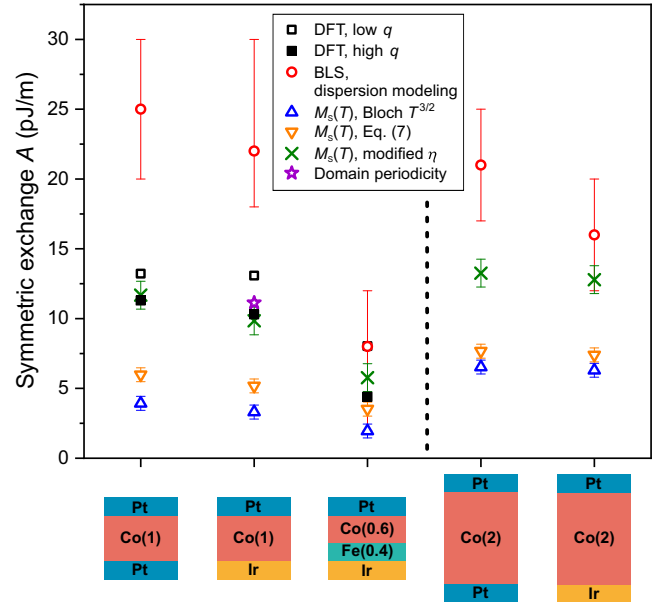


Figure 6. Exchange constant of the samples investigated in this work as obtained from different methods. Values extracted from DFT calculations and from the analysis of the temperature dependence of the magnetization have been renormalized to room temperature. An analysis of the temperature dependence of the magnetization using different models (blue upward and orange downward triangles) consistently delivers smaller values for the exchange constant but incorporating a modified prefactor in Bloch’s $T^{3/2}$ law (green crosses) results in better agreement with results from DFT calculations and dispersion modeling.

tribution probed by the $M_S(T)$ -based methods. In our particular case, also the DFT calculations clearly show that the A values obtained from fits to the low q part lead to significantly higher values for A in comparison to an analysis including the high q part. Thus, a simple parabolic approximation is not justified over the wave vector range probed by the $M_S(T)$ -based methods and an interpretation of the values obtained for A has to be taken with care.

To improve the accuracy of the $M_S(T)$ modelling, it might be needed to consider also higher-order exchange interactions [48, 49], which might be able to capture the more complex wave vector dependence of the exchange energy density. The incorporation of higher-order exchange contributions would, however, drastically increase the effort necessary for an extension of the respective models and disentangling the contributions of different order might even be impossible.

Only the $M_S(T)$ measurements indirectly also probe the higher standing spin-wave (PSSW) modes. Thus, it is of particular interest to further elaborate on the nature of these modes in the ultrathin films under investigation and the resulting consequences on the $M_S(T)$ model, e.g., in Eq. (7). Our assumptions for the PSSW frequencies are based on a micromagnetic continuum theory which

is a rough approximation for ultrathin films of only a few atomic layers in thickness. The work by Pelliciani *et al.* [50] presents an interesting finding on the effect of confinement of these modes. Namely, a reduction of the film thickness towards the ultrathin film regime leads to a renormalization of these modes to lower energies along the out-of-plane direction whereas for the in-plane direction, the dispersion is retained [50]. To test the influence of such a renormalization, we halve the frequencies of the PSSW modes for the Ir/Co(1)/Pt film in the model in Eq. 7 in line with the renormalization factor presented in [50]. With that, we find an increased exchange constant (renormalized to room temperature) of $A = 6.85 \text{ pJ/m}$. This suggests that a modification of the PSSW characteristics can at least in part account for the quantitative differences observed in comparison to the BLS measurements.

In addition, neglecting single particle excitations could render the results base on $M_S(T)$ -measurements inaccurate [32]. Single particle excitations would increase the temperature-dependent magnetization reduction leading again to an underestimation of the exchange constant.

A further error source, which needs to be considered, is the potential presence of a dead layer in the magnetic thin film. The film thickness directly influences the result from the model including PSSW modes for the $M_S(T)$ dependence and the value of the thickness-corrected η [22]. Also, the film thickness governs the dipolar interaction in the spin-wave dispersion relation leading to an additional uncertainty. However, seeing as the magnitude of M_S measured for these ultrathin samples is typically above 1200 kA/m, and largely in line with expected values, we expect any dead layer effects to contribute negligibly in this case [51].

All in all, the analysis and interpretation of $M_S(T)$ data for ultrathin films proves to be far from trivial, as the underlying models contain considerable assumptions that are only partially satisfied. [28].

To conclude, in this work, we have compared different methods for the determination of the Heisenberg exchange in thin magnetic films. Even though this property plays an important role from fundamentals to applications, a thorough understanding of its dependence on interfacial and stack properties is still lacking. Similarly, the differences between the results from the individual methods employed here underline the complexity of the experimental determination of the Heisenberg exchange constant. In general, measurements based on the temperature dependence of the saturation magnetisation tend to provide lower values for the symmetric exchange A compared to an analysis of the spin-wave dispersion relation close to the Brillouin zone origin. Qualitatively, this can be understood by the different spin-wave wave vector ranges probed by the two methods. This causes the methods to be affected differently by the limitations of the parabolic approximation of the dispersion realization.

V. APPENDIX

Film deposition

Multilayer films were deposited on thermally oxidized Si wafers. The active layers are described in Section III and the complete stack structure includes additional seed layers Ta(4)/Pt(5) for optimal texture, and a Pt(2) cap to protect against oxidation. Deposition is performed by DC magnetron sputtering at RT using a ChironTM UHV system (base pressure below 5×10^{-8} torr) from Bestec GmbH.

BLS measurements

BLS measurements have been performed using a wave-vector-resolved setup operated in the backscattering geometry [19]. Here, a laser with a wavelength of $\lambda_L = 532 \text{ nm}$ has been used and the spectral analysis of the inelastically scattered light has been performed utilizing a Tandem-Fabry-Pérot interferometer of Sandercock-type [52]. All BLS measurements have been performed at room temperature and the magnetic field has been applied in the plane of the magnetic film and perpendicular to the plane of incidence of the probing laser light. Wave vector resolution can be achieved by a variation of the angle of incidence, φ , such that the probed spin-wave wave vector equals $k = 4\pi \sin(\varphi)/\lambda_L$.

$M_S(T)$ measurement configurations

The $M(T)$ data has been obtained from measurements of the magnetic moment of the sample as a function of field, at fields beyond sample saturation, for several fixed temperatures. To remove contributions from the substrate, the magnetic moment is fitted to a straight line – with a negative slope owing to the diamagnetic substrate – and is extrapolated towards zero field. Based on the sample size and weight, the magnetization can then be calculated.

As a comparison and in order to verify the appropriateness of this method, additional measurements have been performed in which the magnetization as a function of temperature has been determined at fixed external field. Here, the magnetization can be evaluated incorporating a reference measurement of the bare substrate and the weight and size of the sample under investigation. Figure 7 shows the data obtained from magnetometry measurements at fixed field for different field strength for an Ir/Co(1)/Pt film with the field applied along the film normal (easy axis). The deviations observed for temperatures below 50 K are attributed to residual oxygen and the solid lines are fits of Eq. (7) in the iterative manner described in the main text for which data below $T = 70 \text{ K}$ have been omitted. For these measurements, the fre-

Table I. Summary of the sample properties obtained in this work. For the stack compositions, numbers in brackets denote layer thickness in nm. The values given for $M_S^{(VSM)}$ have been obtained from VSM measurements at room temperature with the field applied along the film normal. The quantities $K_U^{(VSM)}$ and $K_{\text{eff}}^{(VSM)}$ are the uniaxial anisotropy constant and the effective anisotropy constant, respectively. From DFT calculations and by performing a renormalization to room temperature, the values for the Heisenberg exchange constant $A_{\text{DFT}}^{(\text{high } q)}$ and $A_{\text{DFT}}^{(\text{low } q)}$ have been determined for the high and for the low q range, respectively (See Fig. 4). $A_{T^{3/2}}$ has been obtained from the fit of Bloch's $T^{3/2}$ law, whereas $A_{T^{3/2},\text{mod}}$ results from the modified Bloch law using $\eta = 0.3$ for a film thickness of 1 nm and $\eta = 0.17$ for a film thickness of 2 nm. The exchange constant A_{PSSW} is the result of the iterative fit of the model accounting for the contribution of standing spin-wave modes (Eq. (7)), as described in the main text. All values obtained based on fits of Eqs. (4) and (7) have been renormalized to room temperature.

	Pt/Co(1)/Pt	Ir/Co(1)/Pt	Ir/Fe(0.4)/Co(0.6)/Pt	Pt/Co(2)/Pt	Ir/Co(2)/Pt
$M_S^{(VSM)}$ (kA/m)	1434 ± 215	1284 ± 193	1199 ± 180	1330 ± 200	1240 ± 186
$K_U^{(VSM)}$ (MJ/m ³)	1.93 ± 0.29	1.54 ± 0.23	0.86 ± 0.13	0.81 ± 0.12	0.89 ± 0.13
$K_{\text{eff}}^{(VSM)}$ (MJ/m ³)	0.63 ± 0.09	0.50 ± 0.08	-0.05 ± 0.05	-0.12 ± 0.05	0.24 ± 0.05
$A_{\text{DFT}}^{(\text{low } q)}$ (pJ/m ²)	13.22	13.08	8.03	-	-
$A_{\text{DFT}}^{(\text{high } q)}$ (pJ/m ²)	11.32	10.29	4.37	-	-
A_{Disp} (pJ/m ²)	25 ± 5	$22 + 8 / - 4$	$7 + 8 / - 4$	21 ± 4	16 ± 4
$A_{T^{3/2}}$ (pJ/m ²) (Eq. 4)	3.93 ± 0.50	3.31 ± 0.50	1.95 ± 0.50	6.53 ± 0.50	6.30 ± 0.50
A_{PSSW} (pJ/m ²) (Eq. 7)	5.98 ± 0.50	5.18 ± 0.50	3.52 ± 0.50	7.67 ± 0.50	7.40 ± 0.50
$A_{T^{3/2},\text{mod}}$ (pJ/m ²) (Eq. 4)	11.68 ± 1.00	9.84 ± 1.00	5.77 ± 1.00	13.26 ± 1.00	12.79 ± 1.00

quency ω_0 can reliably be estimated using the value of the applied field.

With the thermal occupation being highest for states of the fundamental spin-wave mode, the dipolar gap ω_0 is a crucial parameter for an adequate application of the models in Eqs. (5) and (7). In the context of magnetometry measurements involving the extrapolation method described in the main text, an estimation of ω_0 has been performed by taking the center value of the covered field range, the M_S value estimated from an extrapolation of the experimental $M_S(T)$, the anisotropy field extracted from BLS measurements, and we have used $\omega_0 = \gamma\mu_0(H_{\text{ext}} + H_U - M_S)$ [43] with $\mu_0 H_{\text{ext}} = 300$ mT.

The values calculated for ω_0 are presented in Table II for the different strengths of the applied field used in the experiments together with the estimation used for the analysis of the data obtained from the extrapolation method. Also, the values of the exchange constant which have been obtained from fits of Bloch's $T^{3/2}$ law as well as from the model in Eq. (7) and renormalized to room temperature and are given. The results for the exchange constant are in good agreement substantiating our concept and underlining that both kinds of magnetometry data can equally well be used based on a proper estimation of the dipolar gap ω_0 .

Table II. Estimated values for the dipolar gap ω_0 and resulting exchange constant values renormalized to room temperature for different magnetometry measurements performed with the Ir/Co(1)/Pt film. The quantity $\mu_0 H$ indicates the magnetic field applied in the direct $M_S(T)$ measurements at fixed field which has also been used to calculate $\gamma\mu_0(H_{\text{ext}} + H_U - M_S)$. In the field swept measurement, ω_0 has been estimated based on the covered field range. In all magnetometry measurements, the field has been applied along the film normal.

	$\omega_0/(2\pi)$ (GHz)	$A_{T^{3/2}}$ (pJ/m)	A_{PSSW} (pJ/m)
$\mu_0 H = 100$ mT	20	3.19 ± 0.50	5.06 ± 0.50
$\mu_0 H = 200$ mT	23	3.16 ± 0.50	4.93 ± 0.50
$\mu_0 H = 300$ mT	25	3.35 ± 0.50	5.19 ± 0.50
$\mu_0 H = 400$ mT	28	3.44 ± 0.50	5.28 ± 0.50
Field swept	25	3.31 ± 0.50	5.18 ± 0.50

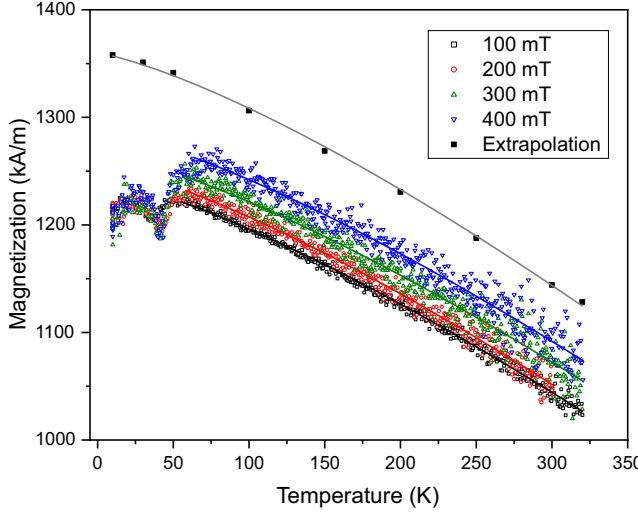


Figure 7. Magnetization as a function of temperature for an Ir/Co(1)/Pt film determined from measurements for different applied field and from the extrapolation (field swept) method. The field is applied along the film normal and deviations at temperatures below 50 K are a trace of residual oxygen. Solid lines are fits according to Eq. (7) results of which are given in Table II.

Effective exchange constant in ferromagnetic bilayer samples

Concerning one of the samples with a ferromagnetic bilayer (Ir/Fe(0.4)/Co(0.6)/Pt), based on the numerical modeling of the dispersion relation, we have verified that the exchange constant of a bilayer can be described using an effective exchange constant in the following manner: First, we have numerically calculated the dispersion relation of the fundamental mode for bilayers $\text{Fe}(t_{\text{Fe}})/\text{Co}(t - t_{\text{Fe}})$ with $t = 1 \text{ nm}$ for an in-plane wave-vector range from $-3000 \text{ rad}/\mu\text{m}$ to $+3000 \text{ rad}/\mu\text{m}$. For that, we have taken for Co a saturation magnetization of $M_{\text{S}}^{(\text{Co})} = 1050 \text{ kA/m}$ and an exchange constant of $A_{\text{Co}} = 20 \text{ pJ/m}$, and for Fe we have assumed $M_{\text{S}}^{(\text{Fe})} = 1600 \text{ kA/m}$ and an exchange constant of $A_{\text{Fe}} = 14 \text{ pJ/m}$. To the obtained data we fit a function of the form $f_{\text{sw}}(k) = \frac{\gamma}{2\pi} \frac{2A}{M} \cdot k^2 = \beta_{\text{num}} k^2$. Hence, the proportionality factor β_{num} is related to an (effective) exchange stiffness $\lambda_{\text{ex,eff}}$ via $\beta_{\text{num}} = \frac{\gamma \mu_0}{2\pi} \lambda_{\text{ex,eff}}$. In order to compare different analytical approaches to the numerically obtained data, we evaluate the following model relations between the exchange constants of the individual layers and the bilayer:

$$\beta_1 = \beta_{\text{Fe}} \cdot \frac{t_{\text{Fe}}}{t} + \beta_{\text{Co}} \cdot \frac{t_{\text{Co}}}{t} \quad (9)$$

$$\beta_2 = \frac{\gamma}{\pi} \frac{(A_{\text{Fe}} + A_{\text{Co}})/2}{(M_{\text{S}}^{(\text{Fe})} \cdot t_{\text{Fe}} + M_{\text{S}}^{(\text{Co})} \cdot t_{\text{Co}})/t} \quad (10)$$

Table III. Effective exchange stiffness for different Fe thickness of the bilayer samples extracted from the dispersion modeling and results from analytical ansatz according to Eqs. (9)-(11). The parameter β_{num} is extracted from the numerical model. Best agreement is achieved with β_3 . The thickness of the Co layer is $t_{\text{Co}} = t - t_{\text{Fe}} = 1 \text{ nm} - t_{\text{Fe}}$

t_{Fe} (nm)	β_{num}	β_1 ($10^{-4} \text{ GHz}/(\text{rad}/\mu\text{m})$)	β_2	β_3
0.2	9.03	9.85	8.21	9.08
0.4	7.36	8.66	7.50	7.76
0.6	6.42	7.47	6.90	6.66

$$\beta_3 = \frac{\gamma}{\pi} \frac{A_{\text{Fe}} \cdot t_{\text{Fe}} + A_{\text{Co}} \cdot t_{\text{Co}}}{M_{\text{S}}^{(\text{Fe})} \cdot t_{\text{Fe}} + M_{\text{S}}^{(\text{Co})} \cdot t_{\text{Co}}}. \quad (11)$$

Here, β_{Fe} and β_{Co} are the curvatures of the dispersion relation obtained from the fit to the numerically evaluated dispersion data for a pure Fe and Co film of 1 nm thickness, respectively.

The resulting values for the different approaches are listed in Table III. It is obvious that a model according to Eq. (11) best describes the numerically obtained exchange parameter for the bilayers. This finding underlines the validity of assuming a parabolic dispersion for the $M(T)$ data analysis also for the case of bilayer samples with an exchange stiffness taken as the ratio of thickness-weighted Heisenberg exchange constant and thickness-weighted saturation magnetization as described by β_3 . We have also verified that the exchange coupling strength between the individual layers only plays a minor role. As long as the coupling is ferromagnetic, no significant influence of the coupling strength could be observed.

Spin-wave density of states for full and parabolic dispersion model

Since every thermally excited magnon reduces the saturation magnetization $M_{\text{S}}(T)$ by $g\mu_{\text{B}}$, the resulting $M_{\text{S}}(T)$ can be expressed as

$$\begin{aligned} M_{\text{S}}(T) &= M_{\text{S}}(0) - g\mu_{\text{B}} \sum_{\vec{k}} n(\vec{k}, T) \\ &= M_{\text{S}}(0) - g\mu_{\text{B}} \int_0^{\infty} N(\omega, T) D(\omega) d\omega. \end{aligned} \quad (12)$$

where $n(\vec{k}, T)$ is the magnon density per unit volume, which, in this case, is expressed as the product of the density of states $D(\omega)$ and the Bose-Einstein distribution factor $N(\omega)$ (Eq. (6)). This is the basis of the model leading to Eqs. (4) and (7). As discussed, for instance,

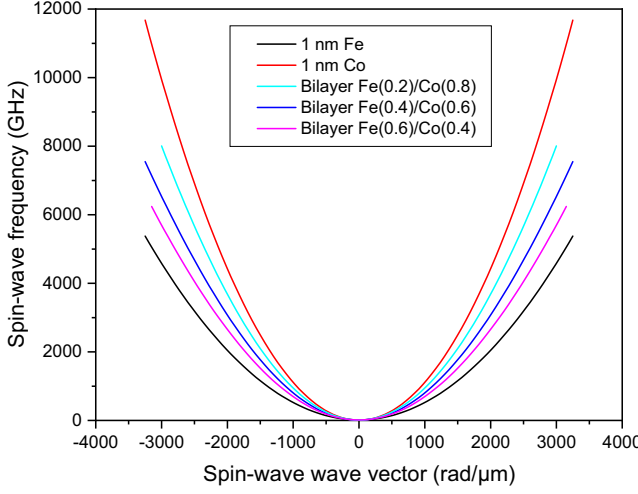


Figure 8. Spin-wave dispersion relation of single Co and Fe film, and of Fe/Co bilayers, obtained based on numerical modeling. The respective material parameters used for the calculations are given in the text. Parabolic fits to the data are used to assess different analytical models for the exchange stiffness in the bilayer samples.

by Bible and Camley [53], the full dispersion based on the Heisenberg model in a 2D square lattice can be described by the relation

$$\omega(k)_{\text{full}} = \omega_0 + \frac{2\gamma\mu_0\lambda_{\text{ex}}}{a^2} (2 - \cos(k_x a) - \cos(k_y a)) \quad (13)$$

where a is the lattice constant of the material and the 2D lattice has been assumed to lie in the xy -plane such that a spin wave has wave vector components k_x and k_y . Correspondingly, the parabolic approximation of the dispersion relation is then given by

$$\omega(k)_{\text{parabolic}} = \omega_0 + \frac{\gamma\mu_0\lambda_{\text{ex}}}{a^2} (k_x^2 + k_y^2) a^2. \quad (14)$$

Both the full model dispersion relation as well as the parabolic approximation are illustrated in Fig. 1a) with parameters used for the calculation given in the main text. In this plot, the blue dashed line indicates a frequency of $f = k_B T/h$ evaluated at room temperature. The increasing deviation between the two models towards larger frequency already hints the increasing deviation of the above-mentioned models for the description of the $M_S(T)$ dependence from the real picture. This can even better be understood by an evaluation of the corresponding density of states (DOS, $\rho(\omega)$) which we have performed numerically. The DOS is given by the number of

available states per frequency interval $d\omega$ at a frequency ω such that

$$\rho(\omega) = \frac{1}{S} \sum_{\vec{k} \in K} \delta(\omega - \omega(\vec{k})) \quad (15)$$

where S and K are the total surface in real and wave vector space, respectively. It is clearly visible that the full Heisenberg model of Eq. (13) leads to a larger DOS compared to the parabolic approximation Eq. (14).

For the calculation of the DOS including DMI, a term linear in the spin-wave wave vector has been added to the dispersion relation with [20, 22, 54]

$$\omega_{\text{DMI}}(k) = \frac{2\gamma}{M_S} D k_x. \quad (16)$$

Clearly, the resulting dispersion modification does not significantly influence the DOS as is visible from the blue curve in Fig. 1b). Thus, the $M_S(T)$ dependence is predicted to be very similar for in-plane field orientation with respect to the film plane (where interfacial DMI contributes to the dispersion relation) and for out-of-plane field orientation, where neglecting the influence of DMI is accurate without approximations.

Lorentz transmission electron microscopy

Lorentz transmission electron microscopy (LTEM) experiments were performed to determine the remanence domain periodicity. An FEI Titan S/TEM operated in Lorentz Fresnel mode at 300 kV, with a dedicated Lorentz lens for focusing the electron beam, was used at a defocus of -1.8 mm. The objective lens located at the sample position was switched off for image acquisition under field-free conditions.

ACKNOWLEDGMENTS

We acknowledge the support of the National Supercomputing Centre (NSCC), Singapore for computational resources. This work was supported by the SpOT-LITE program (Grant No. A18A6b0057), funded by Singapore's RIE2020 initiatives. Funding by the Deutsche Forschungsgemeinschaft within the CRC TRR173 *Spin+X* (Project No. 268565370 (B01)) and within the Priority Program SPP2137 *Skyrmionics* (Project No. 403512431) is gratefully acknowledged.

[1] G. E. Moore, Cramming more components onto integrated circuits, *Electronics* **38**, 114 (1965).

[2] R. W. Keyes, The Impact of Moore's Law, *IEEE Solid-State Circuits Newsletter* **20**, 25 (2006).

[3] M. M. Waldrop, The chips are down for Moore's law, *Nature* **530**, 144 (2016).

[4] S. S. P. Parkin, M. Hayashi, and L. Thomas, Magnetic domain-wall racetrack memory, *Science* **320**, 190 (2008).

[5] A. Fert, V. Cros, and J. Sampaio, Skyrmions on the track, *Nature Nanotechnology* **8**, 152 (2013).

[6] W. Jiang, P. Upadhyaya, W. Zhang, G. Yu, M. B. Jungfleisch, F. Y. Fradin, J. E. Pearson, Y. Tserkovnyak, K. L. Wang, O. Heinonen, S. G. E. te Velthuis, and A. Hoffmann, Magnetism. Blowing magnetic skyrmion bubbles, *Science* **349**, 283 (2015).

[7] A. Soumyanarayanan, N. Reyren, A. Fert, and C. Panagopoulos, Emergent phenomena induced by spin-orbit coupling at surfaces and interfaces, *Nature* **539**, 509 (2016).

[8] W. Kang, Y. Huang, C. Zheng, W. Lv, N. Lei, Y. Zhang, X. Zhang, Y. Zhou, and W. Zhao, Voltage Controlled Magnetic Skyrmion Motion for Racetrack Memory, *Scientific Reports* **6**, 23164 (2016).

[9] B. Dieny, I. L. Prejbeanu, K. Garello, P. Gambardella, P. Freitas, R. Lehndorff, W. Raberg, U. Ebels, S. O. Demokritov, J. Akerman, A. Deac, P. Pirro, C. Adelmann, A. Anane, A. V. Chumak, A. Hirohata, S. Mangin, S. O. Valenzuela, M. C. Onbaşlı, M. d'Aquino, G. Prenat, G. Finocchio, L. Lopez-Diaz, R. Chantrell, O. Chubykalo-Fesenko, and P. Bortolotti, Opportunities and challenges for spintronics in the microelectronics industry, *Nature Electronics* **3**, 446 (2020).

[10] X. Zhang, Y. Zhou, K. M. Song, T.-E. Park, J. Xia, M. Ezawa, X. Liu, W. Zhao, G. Zhao, and S. Woo, Skyrmion-electronics: writing, deleting, reading and processing magnetic skyrmions toward spintronic applications, *Journal of Physics: Condensed Matter* **32**, 143001 (2020).

[11] X. S. Wang, H. Y. Yuan, and X. R. Wang, A theory on skyrmion size, *Communications Physics* **1**, 31 (2018).

[12] I. Dzyaloshinsky, A thermodynamic theory of "weak" ferromagnetism of antiferromagnetics, *Journal of Physics and Chemistry of Solids* **4**, 241 (1958).

[13] T. Moriya, Anisotropic Superexchange Interaction and Weak Ferromagnetism, *Physical Review* **120**, 91 (1960).

[14] C. Moreau-Luchaire, C. Mouta S, N. Reyren, J. Sampaio, C. A. F. Vaz, N. van Horne, K. Bouzehouane, K. Garcia, C. Deranlot, P. Warnicke, P. Wohlhüter, J.-M. George, M. Weigand, J. Raabe, V. Cros, and A. Fert, Additive interfacial chiral interaction in multilayers for stabilization of small individual skyrmions at room temperature, *Nature Nanotechnology* **11**, 444 (2016).

[15] A. Soumyanarayanan, M. Raju, A. L. Gonzalez Oyarce, A. K. C. Tan, M.-Y. Im, A. P. Petrović, P. Ho, K. H. Khoo, M. Tran, C. K. Gan, F. Ernult, and C. Panagopoulos, Tunable room-temperature magnetic skyrmions in Ir/Fe/Co/Pt multilayers, *Nature Materials* **16**, 898 (2017).

[16] S. Woo, K. Litzius, B. Krüger, M.-Y. Im, L. Caretta, K. Richter, M. Mann, A. Krone, R. M. Reeve, M. Weigand, P. Agrawal, I. Lemesh, M.-A. Mawass, P. Fischer, M. Kläui, and G. S. D. Beach, Observation of room-temperature magnetic skyrmions and their current-driven dynamics in ultrathin metallic ferromagnets, *Nature Materials* **15**, 501 (2016).

[17] P. Pirro, V. I. Vasyuchka, A. A. Serga, and B. Hillebrands, Advances in coherent magnonics, *Nature Reviews Materials* **10.1038/s41578-021-00332-w** (2021).

[18] T. Böttcher, K. Lee, F. Heussner, S. Jaiswal, G. Jakob, M. Kläui, B. Hillebrands, T. Bracher, and P. Pirro, Heisenberg Exchange and Dzyaloshinskii–Moriya Interaction in Ultrathin Pt(W)/CoFeB Single and Multilayers, *IEEE Transactions on Magnetics* **57**, 1600207 (2021).

[19] T. Sebastian, K. Schultheiss, B. Obry, B. Hillebrands, and H. Schultheiss, Micro-focused Brillouin light scattering: Imaging spin waves at the nanoscale, *Frontiers in Physics* **3**, 1589 (2015).

[20] M. Belmeguenai, J.-P. Adam, Y. Roussigné, S. Eimer, T. Devolder, J.-V. Kim, S. M. Cherif, A. A. Stashkevich, and A. Thiaville, Interfacial Dzyaloshinskii–Moriya interaction in perpendicularly magnetized Pt/Co/A_x ultrathin films measured by Brillouin light spectroscopy, *Physical Review B* **91**, 180405(R) (2015).

[21] K. Di, V. L. Zhang, H. S. Lim, S. C. Ng, M. H. Kuok, X. Qiu, and H. Yang, Asymmetric spin-wave dispersion due to Dzyaloshinskii–Moriya interaction in an ultrathin Pt/CoFeB film, *Applied Physics Letters* **106**, 052403 (2015).

[22] H. T. Nembach, J. M. Shaw, M. Weiler, E. Jué, and T. J. Silva, Linear relation between Heisenberg exchange and interfacial Dzyaloshinskii–Moriya interaction in metal films, *Nature Physics* **11**, 825 (2015).

[23] K. Shahbazi, J.-V. Kim, H. T. Nembach, J. M. Shaw, A. Bischof, M. D. Rossell, V. Jeudy, T. A. Moore, and C. H. Marrows, Domain-wall motion and interfacial Dzyaloshinskii–Moriya interactions in Pt/Co/Ir(*t*_{Ir})/Ta multilayers, *Physical Review B* **99**, 094409 (2019).

[24] B. A. Kalinikos and A. N. Slavin, Theory of dipole-exchange spin wave spectrum for ferromagnetic films with mixed exchange boundary conditions, *Journal of Physics C: Solid State Physics* **19**, 7013 (1986).

[25] B. Hillebrands, Spin-wave calculations for multilayered structures, *Physical Review B* **41**, 530 (1990).

[26] M. P. Kostylev, Interface boundary conditions for dynamic magnetization and spin wave dynamics in a ferromagnetic layer with the interface Dzyaloshinskii–Moriya interaction, *Journal of Applied Physics* **115**, 233902 (2014).

[27] J. A. C. Bland, ed., *Ultrathin Magnetic Structures I: An Introduction to the Electronic, Magnetic and Structural Properties* (Springer-Verlag Berlin Heidelberg, Berlin, Heidelberg, 2005).

[28] R. P. Erickson and D. L. Mills, Thermodynamics of thin ferromagnetic films in the presence of anisotropy and dipolar coupling, *Physical Review B* **44**, 11825 (1991).

[29] C. A. F. Vaz, J. A. C. Bland, and G. Lauhoff, Magnetism in ultrathin film structures, *Reports on Progress in Physics* **71**, 056501 (2008).

[30] F. Bloch, Zur Theorie des Ferromagnetismus, *Zeitschrift für Physik* **61**, 206 (1930).

[31] I. A. Yastremsky, O. M. Volkov, M. Kopte, T. Kosub, S. Stienien, K. Lenz, J. Lindner, J. Fassbender, B. A. Ivanov, and D. Makarov, Thermodynamics and Exchange Stiffness of Asymmetrically Sandwiched Ultrathin Ferromagnetic Films with Perpendicular Anisotropy, *Physical Review Applied* **12**, 064038 (2019).

[32] T. Maeda, H. Yamauchi, and H. Watanabe, Spin Wave Resonance and Exchange Parameters in fcc Fe-Ni Alloys, *Journal of the Physical Society of Japan* **35**, 1635 (1973).

[33] M. H. Seavey and P. E. Tannenwald, Direct Observation of Spin-Wave Resonance,

Physical Review Letters **1**, 168 (1958).

[34] W. Kipferl, M. Dumm, P. Kotissek, F. Steinbauer, and G. Bayreuther, Bloch's law for epitaxial ultrathin dot arrays with uniaxial magnetic anisotropy, Journal of Applied Physics **95**, 7417 (2004).

[35] S. Cojocaru, A. Naddeo, and R. Citro, Modification of the Bloch law in ferromagnetic nanostructures, EPL (Europhysics Letters) **106**, 17001 (2014).

[36] N. D. Mermin and H. Wagner, Absence of Ferromagnetism or Antiferromagnetism in One- or Two-Dimensional Isotropic Heisenberg Models, Physical Review Letters **17**, 1133 (1966).

[37] R. Moreno, R. F. L. Evans, S. Khmelevskyi, M. C. Muñoz, R. W. Chantrell, and O. Chubykalo-Fesenko, Temperature-dependent exchange stiffness and domain wall width in Co, Physical Review B **94**, 104433 (2016).

[38] P. Blaha, K. Schwarz, F. Tran, R. Laskowski, G. K. H. Madsen, and L. D. Marks, Wien2k: An apw+lo program for calculating the properties of solids, The Journal of Chemical Physics **152**, 074101 (2020).

[39] R. Laskowski, G. K. H. Madsen, P. Blaha, and K. Schwarz, Magnetic structure and electric-field gradients of uranium dioxide: An ab initio study, Phys. Rev. B **69**, 140408 (2004).

[40] J. P. Perdew, K. Burke, and M. Ernzerhof, Generalized gradient approximation made simple, Phys. Rev. Lett. **77**, 3865 (1996).

[41] L. M. Sandratskii, Noncollinear magnetism in itinerant-electron systems: Theory and applications, Advances in Physics **47**, 91 (1998).

[42] Xiaoye Chen, Ming Lin, Jian Feng Kong, Hui Ru Tan, Anthony K.C. Tan, Soong-Geun Je, Hang Khume Tan, Khoong Hong Khoo, Mi-Young Im, and Anjan Soumyanarayanan, Unveiling the emergent traits of chiral spin textures in magnetic multilayers, Private Communication.

[43] C. Kittel, On the Theory of Ferromagnetic Resonance Absorption, Physical Review **73**, 155 (1948).

[44] K. von Bergmann, S. Heinze, M. Bode, E. Y. Vedmedenko, G. Bihlmayer, S. Blügel, and R. Wiesendanger, Observation of a complex nanoscale magnetic structure in a hexagonal Fe monolayer, Physical Review Letters **96**, 167203 (2006).

[45] A. Vansteenkiste, J. Leliaert, M. Dvornik, M. Helsen, F. Garcia-Sanchez, and B. van Waeyenberge, The design and verification of MuMax3, AIP Advances **4**, 107133 (2014).

[46] P. J. Metaxas, J. P. Jamet, A. Mougin, M. Cormier, J. Ferré, V. Baltz, B. Rodmacq, B. Dieny, and R. L. Stamps, Creep and flow regimes of magnetic domain-wall motion in ultrathin Pt/Co/Pt films with perpendicular anisotropy, Physical Review Letters **99**, 217208 (2007).

[47] P. M. Shepley, H. Tunnicliffe, K. Shahbazi, G. Burnell, and T. A. Moore, Magnetic properties, domain-wall creep motion, and the Dzyaloshinskii-Moriya interaction in Pt/Co/Ir thin films, Physical Review B **97**, 10.1103/PhysRevB.97.134417 (2018).

[48] S. Banerjee, J. Rowland, O. Erten, and M. Randeria, Enhanced Stability of Skyrmions in Two-Dimensional Chiral Magnets with Rashba Spin-Orbit Coupling, Physical Review X **4**, 031045 (2014).

[49] M. Gutzeit, S. Haldar, S. Meyer, and S. Heinze, Trends of higher-order exchange interactions in transition metal trilayers, Physical Review B **104**, 024420 (2021).

[50] J. Pelliciari, S. Lee, K. Gilmore, J. Li, Y. Gu, A. Barbour, I. Jarrire, C. H. Ahn, F. J. Walker, and V. Bisogni, Tuning spin excitations in magnetic films by confinement, Nature Materials **20**, 188 (2021).

[51] H. K. Tan, R. J. J. Lim, H. L. Seng, J. Shambugam, H. Y. Y. Ko, X. M. Cheng, V. Putra, Z. X. Xing, A. Soumyanarayanan, and P. Ho, Intermixing induced anisotropy variations in CoB-based chiral multilayer films, Journal of Physics D: Applied Physics **54**, 354003 (2021).

[52] B. Hillebrands, Progress in multipass tandem Fabry-Perot interferometry: I. A fully automated, easy to use, self-aligning spectrometer with increased stability and flexibility, Review of Scientific Instruments **70**, 1589 (1999).

[53] J. J. Bible and R. E. Camley, Focusing of high-wavevector magnons, Physical Review B **95**, 224412 (2017).

[54] K. Di, V. L. Zhang, H. S. Lim, S. C. Ng, M. H. Kuok, J. Yu, J. Yoon, X. Qiu, and H. Yang, Direct observation of the Dzyaloshinskii-Moriya interaction in a Pt/Co/Ni film, Physical Review Letters **114**, 047201 (2015).